Article

NiSe$_2$/Ag$_3$PO$_4$ Nanocomposites for Enhanced Visible Light Photocatalysts for Environmental Remediation Applications

Madeeha Rani [1], Maida Murtaza [1], Aneeqa Amjad [1], Manzar Zahra [2], Amir Waseem [1,*]
and Aiyeshah Alhodaib [3,*]

[1] Department of Chemistry, Faculty of Natural Sciences, Quaid-i-Azam University, Islamabad 45320, Pakistan
[2] Department of Chemistry, Faculty of Basic Sciences, Lahore Garrison University, Lahore 94777, Pakistan
[3] Department of Physics, College of Science, Qassim University, Buraydah 51452, Saudi Arabia
[*] Correspondence: amir@qau.edu.pk (A.W.); ahdieb@qu.edu.sa (A.A.)

Abstract: This study investigated the use of NiSe$_2$/Ag$_3$PO$_4$ nanocomposite catalysts for the photocatalytic degradation of RhB and BPA pollutants. Samples of pure NiSe$_2$, Ag$_3$PO$_4$, and NiSe$_2$/Ag$_3$PO$_4$ composites with varying NiSe$_2$ (10%, 20%, and 30%) proportions were synthesized using hydrothermal techniques. The 20% NiSe$_2$/Ag$_3$PO$_4$ composite showed the greatest photocatalytic efficiency for both RhB and BPA degradation. The study also examined the impact of various factors, such as the initial concentration of dye, catalyst amount, pH, and reaction time, on the photodegradation process. The 20% NiSe$_2$/Ag$_3$PO$_4$ catalyst effectively degraded 10 ppm RhB in 20 min and 20 ppm BPA in 30 min. The physical properties of the samples were examined using SEM, PXRD, and energy-dispersive X-ray spectroscopy. The cycling runs of 20% NiSe$_2$/Ag$_3$PO$_4$ also exhibited improved stability compared to Ag$_3$PO$_4$, with a degradation rate of 99% for RhB and BPA. The combination and synergistic effect of NiSe$_2$ and Ag$_3$PO$_4$ played a vital role in enhancing the stability of the photocatalysts. Both the RhB and BPA photodegradation followed pseudo-first-order kinetic models with rate constants of 0.1266 min^{-1} and 0.2275 min^{-1}, respectively. The study also presented a Z-scheme reaction mechanism to elucidate the process of photodegradation exhibited by the composites after active species capture experiments, which showed that superoxide anion radicals and holes were responsible for the photodegradation.

Keywords: bisphenol A; rhodamine B; degradation; photocatalysis; nickel selenide

1. Introduction

Over the past few years, soil and freshwater quality has declined as a result of the increased use of both inorganic and organic substances, in addition to industrialization, overcrowding, and overpopulation [1–4]. Dyes, which are commonly used in daily life, pose a danger to plants, humans, and animals, and their release into the environment can be damaging [5–8]. Rhodamine B and bisphenol A are the two main pollutants present in wastewater.

Rhodamine B is an artificial coloring agent that is commonly used in the food and textile industries to enhance the color of products. Unfortunately, RhB is also present in wastewater. Because it is not biodegradable, RhB can contaminate the environment by discharging harmful and cancer-causing substances into water. This can result in serious environmental pollution issues [9]. Exposure to rhodamine B can cause skin hypersensitivity, respiratory problems, gastrointestinal irritation, and even blindness (if ingested).

Bisphenol A (BPA) is mainly utilized in the large-scale manufacturing of polycarbonate polymers. This chemical can be found in various products, such as water bottles, eyewear, shatterproof glass, epoxy resins, metal food cans, bottle lids, and water supply pipes [10]. Growing concerns are being raised about the potential adverse impacts of BPA exposure on the developing brains and prostate glands of fetuses, newborns, and children, as well as

its impact on their behavior. BPA is commonly consumed through contaminated food and water. As a result of its extensive use and increasing discharge into the environment, BPA has emerged as a new form of environmental pollution [11]. One way to treat wastewater that contains RhB and other pollutants is using advanced oxidation methods, such as heterogeneous semiconductor photocatalysis [12]. Ag_3PO_4 exhibits remarkable visible light-activated photocatalytic properties, enabling it to efficiently degrade various water pollutants. Its exceptional photocatalytic features include high quantum efficiency (>90% at >420 nm), potent oxidative capacity, minimal solubility in water, and the ability to attract or repel electrons and holes to or from phosphate anions [13,14]. The utilization of Ag_3PO_4 as a standalone photocatalyst poses difficulties due to its susceptibility to photochemical instability, which is caused by the reduction in Ag cations to elemental Ag upon exposure to light. One solution to this issue is to create heterogeneous semiconductor structures, which can improve both the photochemical stability and photocatalytic efficiency of Ag_3PO_4 [15].

Ag_3PO_4 has been combined with other semiconductors that can be driven by visible light, such as ZnS, ZnO, CdS, TiO_2, and WO_3, to boost its photocatalytic performance and photochemical stability for the degradation of specific pollutants [16]. $NiSe_2/Ag_3PO_4$ nanocomposites exhibit improved photocatalytic activity, especially in removing RhB and BPA. This removal process relies on a mechanism of heterojunction, which involves the migration of photoinduced electrons from the Ag_3PO_4 conduction band to the valence band of $NiSe_2$, in order to minimize the amount of charge carrier recombination [17]. Chalcogenide-based compounds, such as NiS_2, Bi_2S_3 and Sb_2S_3, have recently gained attention as promising photocatalysts for visible light-driven applications due to their narrow band gap of approximately 1.6–2.5 eV and their high photocatalytic efficiency. These materials are capable of absorbing visible light, which allows for efficient energy conversion and enhanced charge transfer kinetics, leading to improved water oxidation mechanisms by electron-hole pairs [18]. Sulfide-based materials exhibit high charge carrier mobility due to their unique electronic structures, which allows for the efficient separation of photogenerated electron-hole pairs, leading to high photocatalytic activity. In addition, sulfide-based materials are generally chemically stable under harsh reaction conditions and can withstand high temperatures and pressures, as well as corrosive environments. This makes them highly suitable for use in photocatalytic reactions [19]. The high photocatalytic activity of chalcogenide-based compounds can be attributed to their unique electronic and structural properties, such as band gap, surface area, and crystallinity. Additionally, these materials are chemically stable and abundant, making them cost-effective and sustainable alternatives to other photocatalysts. $NiSe_2$ is an attractive n-type photocatalyst that is driven by visible light, which possesses a band gap of 1.98 eV and is capable of responding to nearly the entire visible spectrum. It can be combined with other semiconductors to effectively eliminate water pollutants. In recent times, there has been a surge of interest in transition metal dichalcogenides (TMDCs), including $NiSe_2$, due to their active chalcogenide atoms, appropriate band gap energy, low costs, and exceptional catalytic activity [20–22]. Nickel selenide, which is a type of TMDC, has been utilized in supercapacitors, sodium-ion batteries, and electrocatalytic hydrogen evolution. Crystal $NiSe_2$ can exist in both the cubic and orthorhombic phases at different temperatures [23,24]. The electronic configuration of nickel ($3d^8$, $4s^2$) and the slight difference in electronegativity between nickel ($\chi = 1.9$) and selenium ($\chi = 2.4$) enable the formation of different nickel selenides, including non-stoichiometric compounds. The cubic pyrite structure of $NiSe_2$ consists of dumbbell-shaped Se_2 units located between two nickel atoms.

The band gap energy of nickel selenide is suitable for absorbing visible light but its photocatalytic activity is not as efficient as expected because of the electron and hole pair re-combination. Composite formation is an effective method for enhancing the photocatalytic activity of nickel selenide and expanding its light absorption spectrum from UV to the visible range. This technique involves the introduction of a new band into the original band or the modification of the valence band (VB) or conduction band (CB) of the composite material [25–27]. In this research, we created a composite material by combining $NiSe_2$

with silver phosphate and successfully used it for the degradation of dyes (using RhB as a model dye) and BPA.

2. Results and Discussion

2.1. Powder X-ray Diffraction (PXRD)

The X-ray diffraction (XRD) patterns of $NiSe_2$ and Ag_3PO_4 were compared and it was observed that $NiSe_2$ had diffraction peaks at 2θ values of 29.9°, 33.58°, 36.9°, 50.8°, 55.58°, and 57.8°, which corresponded to the cubic phase of $NiSe_2$ (JCPDS No.00-011-0552; space group = Pa3; a = 5.9604 Å), while Ag_3PO_4 had diffraction peaks at 2θ values of 20.8°, 29.8°, 33.3°, 36.6°, 47.9°, 52.5°, and 57.2°, which corresponded to the cubic structure of Ag_3PO_4 (JCPDS No.00-006-0505; space group = P4 3n; a = 6.0130 Å). The XRD pattern of the 20% $NiSe_2$/Ag_3PO_4 composite indicated that the synthesis was successful as it exhibited a mixture of $NiSe_2$ and Ag_3PO_4, as shown in Figure 1. The Ag_3PO_4 powder obtained through the hydrothermal process had distinct diffraction peaks and was well crystallized. Due to the smaller crystallite size of $NiSe_2$, its peaks were less sharp and larger in comparison to those of Ag_3PO_4 [28]. The application of the Debye–Scherrer equation allowed us to calculate the sizes of the crystallites present in $NiSe_2$, Ag_3PO_4, and the 20% $NiSe_2$/Ag_3PO_4 composite. The results showed that the crystallite size of $NiSe_2$ was 22.38 nm, while that of Ag_3PO_4 was 86.52 nm and that of the composite was 47.73 nm.
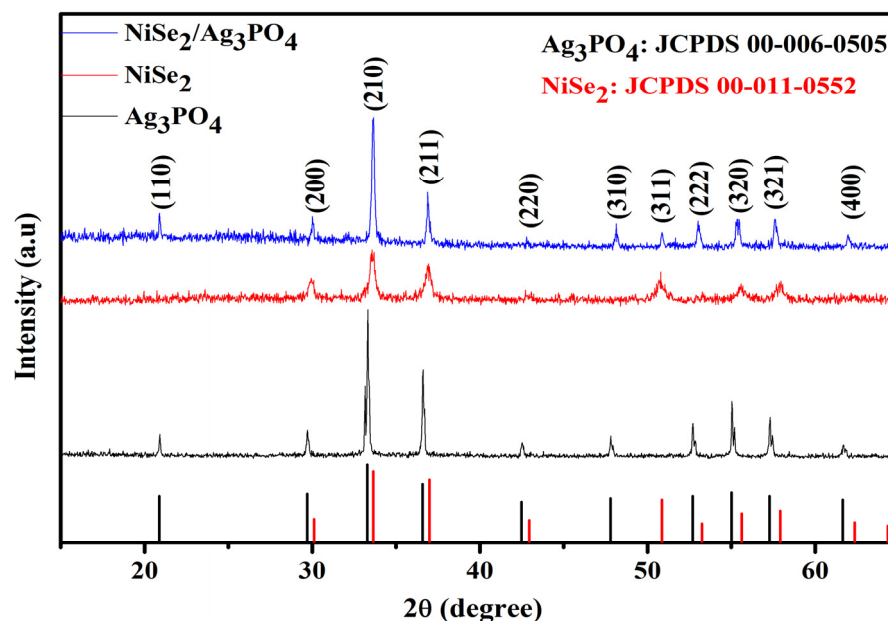
$$D = K \cdot \lambda / (\beta \cdot \cos \theta)$$

Figure 1. The powder XRD patterns of the $NiSe_2$, Ag_3PO_4, and 20% $NiSe_2$/Ag_3PO_4 composite samples.

2.2. Scanning Electron Microscopy (SEM)

FESEM was utilized to analyze the size and morphology of the synthesized samples. The images of $NiSe_2$ showed larger numbers of nanoflakes at various magnifications, as presented in Figure 2a,b. On the other hand, pure Ag_3PO_4 particles formed globular shapes and showed polyhedral morphology with interstitial spaces, as seen in Figure 2c,d. Figure 2e,f shows that the particles of $NiSe_2$ were attached to the surface of Ag_3PO_4 in the 20% $NiSe_2$/Ag_3PO_4 composite, possibly due to the accumulation of $NiSe_2$ filling these spaces. The arrangement of $NiSe_2$ particles on the surface of Ag_3PO_4 was uniform, as shown in Figure 2e,f.
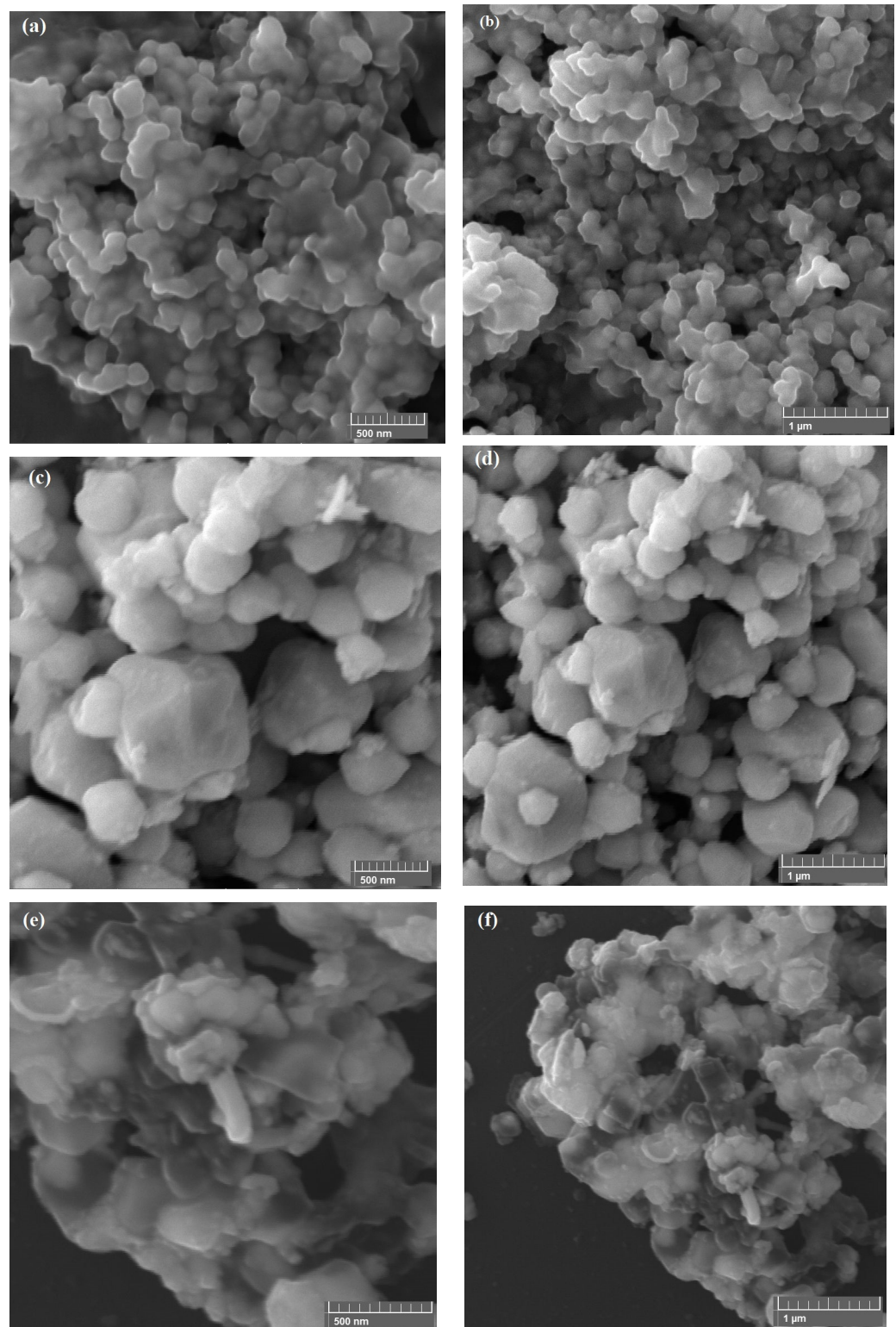
Figure 2. The SEM images of $NiSe_2$ (**a**,**b**), Ag_3PO_4 (**c**,**d**), and the 20% $NiSe_2/Ag_3PO_4$ composite (**e**,**f**) at different resolutions.

2.3. Energy-Dispersive X-ray Spectroscopy

The elemental compositions of pure $NiSe_2$, Ag_3PO_4, and 20% $NiSe_2/Ag_3PO_4$ particles were estimated from the EDX spectrum, as displayed in Figure 3. The EDX analysis of Ag_3PO_4 revealed the presence of Ag (76.83 wt%), P (7.5 wt%), and O (15.6 wt%). $NiSe_2$ showed the presence of Ni (35.91 wt%) and Se (64.09 wt%). On the other hand, the 20%

$NiSe_2/Ag_3PO_4$ composite showed the presence of Ag (61.81 wt%), P (6 wt%), Ni (7.18 wt%), Se (12.4 wt%), and O (12.48 wt%). All of these elements were present in the composite, confirming the success of its synthesis.
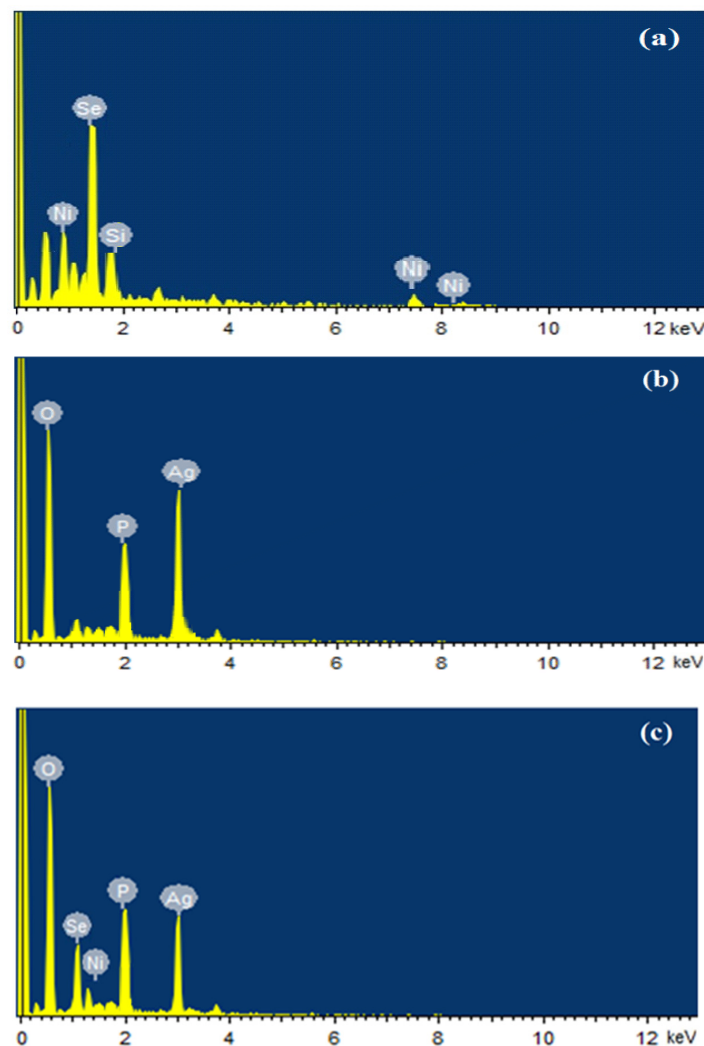

Figure 3. The EDX images of $NiSe_2$ (**a**), Ag_3PO_4 (**b**), and the 20% $NiSe_2/Ag_3PO_4$ composite (**c**).

2.4. Optical Study and Band Gap Calculation

A mathematical expression known as the Tauc equation correlates the absorption spectra of semiconductor nanomaterials with their band gap energy. According to this equation, once a certain level of energy is absorbed, electrons transition from the valence band to the conduction band [29].

$$(\alpha h\upsilon) = k\,(h\upsilon - E_g)^n$$

The Tauc equation relates the energy of the band gaps (E_g) in semiconductor nanomaterials to the energy of the photons ($h\upsilon$) and the coefficient of absorption (α), which is obtained using the Beer–Lambert law. The equation also involves a tailing parameter (k) that is independent of energy and the type of transition (n), which is 1/2 for direct transitions and 2 for indirect transitions [30]. The determination of the band gap energy (E_g) can be achieved by extrapolating the linear section of a graph plotting the relationship between the square of the absorption coefficient (α) and the photon energy ($h\upsilon$) in the UV-Vis range (200–800 nm). However, several factors, such as doping, annealing treatments, grain size, and transition type (direct or indirect), can affect the E_g value [31]. The band gap energies of $NiSe_2$ and Ag_3PO_4 were 1.98 and 2.36 eV, respectively, while the band gap energy of the

20% $NiSe_2/Ag_3PO_4$ composite was 2.17 eV. The Tauc plots of the $NiSe_2$, Ag_3PO_4, and 20% $NiSe_2/Ag_3PO_4$ samples are presented in Figure 4a–c, from which the band gap energies were determined by extrapolating the linear parts of the graphs.
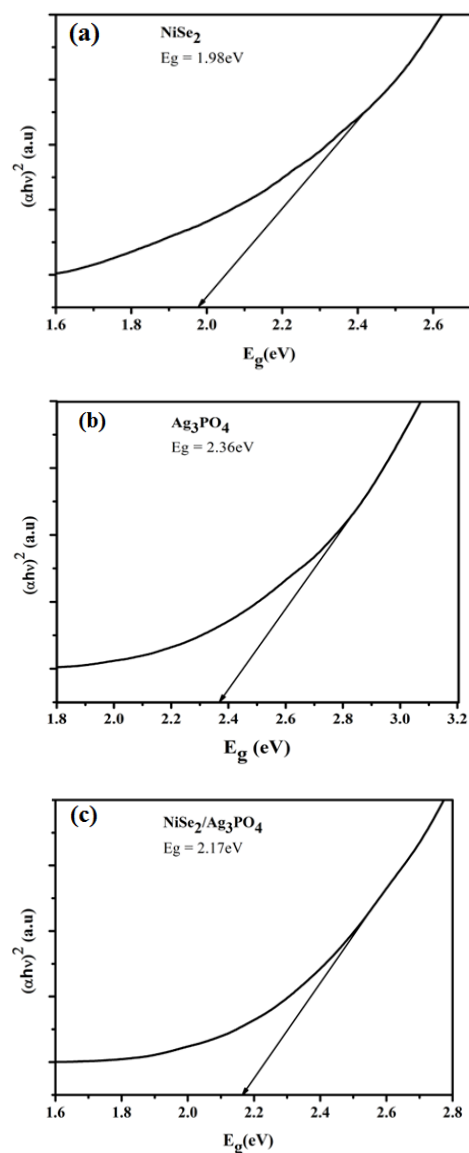

Figure 4. The Tauc plots of (**a**) $NiSe_2$, (**b**) Ag_3PO_4, and the (**c**) 20% $NiSe_2/Ag_3PO_4$ composite.

2.5. Rhodamine B Optimization Studies

The main goal of this research was to investigate new methods for improving the effectiveness of photodegradation in the breakdown of rhodamine B by examining different factors, such as pH, catalyst amount, and dye concentration (RhB).

2.5.1. Selection of Appropriate Catalysts for RhB Degradation

To evaluate the photocatalytic activity of the synthesized samples, 20 mg of each photocatalyst was added to 30 mL of a solution containing rhodamine B (RhB) at a concentration of 5 ppm. The degradation of RhB was then measured using UV-visible spectrophotometry [32]. To assess the photocatalytic efficiency of the photocatalysts, a mixture containing 20 mg of each photocatalyst and 30 mL of rhodamine B (RhB) solution at a 5 ppm concentration was stirred under visible light for 30 min while the temperature was maintained at 25 °C. The UV-visible absorption spectra of RhB were collected between 200 and 600 nm during the photocatalytic experiments and then any reductions in the

RhB characteristic peaks were measured to determine the RhB degradation efficiency. The performance of the catalysts was evaluated by comparing their photocatalytic activity, and the catalyst with the highest dye degradation efficiency was selected. According to the findings, as the percentage of NiSe$_2$ in the composite increased, there was a corresponding rise in its photocatalytic activity up to a limit of 20%, which then decreased slightly with the further increase to 30%. The 20% NiSe$_2$/Ag$_3$PO$_4$ composite exhibited the most significant photocatalytic activity for degrading RhB, outperforming pure NiSe$_2$, Ag$_3$PO$_4$, and the 10% and 30% NiSe$_2$/Ag$_3$PO$_4$ composites. Thus, it was concluded that the 20% NiSe$_2$/Ag$_3$PO$_4$ composite would be a promising photocatalyst for the degradation of RhB. Figure 5a illustrates the photocatalytic activity of the NiSe$_2$/Ag$_3$PO$_4$ composites with different NiSe$_2$ contents.
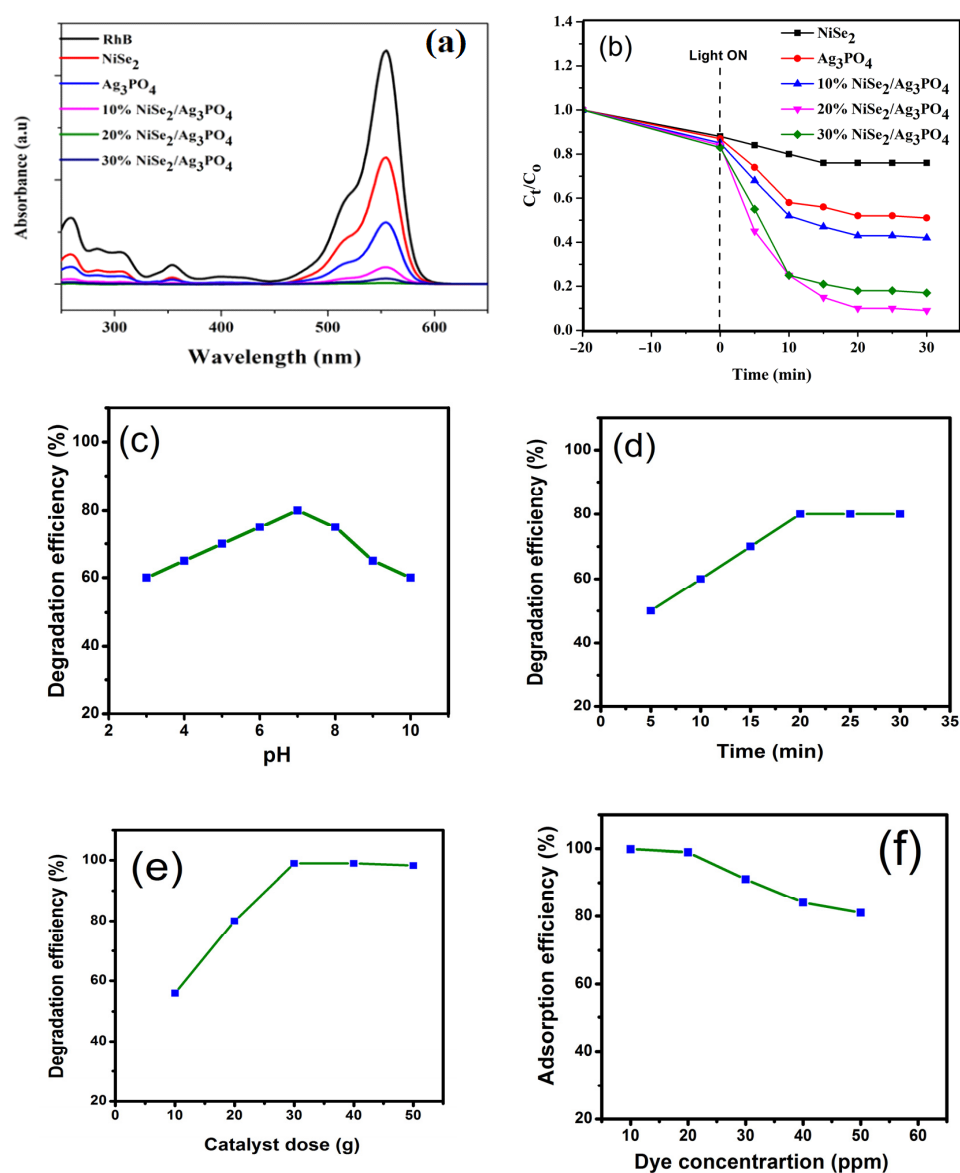

Figure 5. The optimization studies of RhB degradation: (**a**) the UV-Vis spectra for catalyst selection (conditions: catalyst dose = 20 mg; RhB = 5 ppm; time = 30 min); (**b**) the degradation efficiency of various photocatalysts as a function of irradiation time (the other conditions were the same as in (**a**)); (**c**) pH; (**d**) reaction time; (**e**) catalyst dose; (**f**) RhB concentration.

2.5.2. Effect of pH on the Degradation of Rhodamine B

The degradation mechanism is significantly influenced by the pH level of a solution, although it varies depending on the source of wastewater. In this study, sodium hydroxide and hydrochloric acid solutions were used to adjust the pH of the RhB solution. The photodegradation of RhB was performed with a catalyst dose of 20 mg in 30 mL of a 10 ppm RhB solution at pH values ranging from 3 to 11 for 30 min at a temperature of 25 °C. The RhB concentration in the clear solution was measured using a UV-Vis spectrophotometer. Figure 5c shows that the highest efficiency of RhB degradation was achieved by the 20% $NiSe_2/Ag_3PO_4$ photocatalyst at pH 7. At pH 5.4, the Ag_3PO_4 catalyst's surface was neutral; however, its surface charge became negative in alkaline media and positive in acidic media. The degradation efficiency of rhodamine B was found to be the highest in neutral solutions with a pH of 7, but it decreased in alkaline media. This could be attributed to the fact that rhodamine B is a cationic dye that degrades slightly in basic solutions (above pH 7). When the pH value exceeded 5.4, the surface of the catalysts became negatively charged, likely due to the reduction in silver ions in the silver phosphate to elemental silver. This resulted in a decrease in the active sites of the catalysts and reduced the efficiency of the degradation process.

2.5.3. Reaction Time Optimization for the Photodegradation of Rhodamine B

The study investigated the optimal duration for the degradation of RhB using the 20% $NiSe_2/Ag_3PO_4$ photocatalyst. A degradation experiment was conducted at pH 7, using 20 mg of the photocatalyst and exposure times varying between 0–30 min at 25 °C. The results showed that with an increase in exposure time, there was a rapid decrease in the RhB absorption peak and changes in the color of the dye solution. Longer exposure times led to higher degradation efficiency as electrons transitioned faster from the valence band to the conduction band. The RhB was completely degraded after 20 min of exposure, as shown in Figure 5d.

2.5.4. Catalyst Dose Optimization for the Photodegradation of Rhodamine B

To estimate the cost and determine the amount of photocatalyst needed for maximum efficiency, a study was conducted using a 10 ppm RhB solution at pH 7 for 20 min at a temperature of 25 °C. It was found that the optimal conditions were a catalyst dose of 10–50 mg, with the percentage of degradation increasing with the increase in catalyst dose. Figure 5e shows that the highest degradation efficiency was obtained when the catalyst dose was 30 mg. This could be attributed to the increase in the number of active sites of the catalyst, which promoted the formation of more reactive radicals, such as superoxide anion and hydroxyl, resulting in increased degradation efficiency.

2.5.5. Dye Concentration Optimization for the Photodegradation of Rhodamine B

The effect of RhB concentration on the efficiency of its degradation was investigated by testing various concentrations, ranging from 10 ppm to 50 ppm, under visible light exposure. The results showed that the photodegradation process was slower at higher RhB concentrations. This could be attributed to the reduction in active sites of the catalysts, which was caused by the larger number of dye molecules adsorbed on the catalyst surfaces. Furthermore, at high dye concentrations, the catalysts could self-absorb the dye, obstructing light from reaching the catalyst surfaces. These factors led to the inhibition of the formation of highly oxidative $O_2^{\bullet-}$ and, as a result, decreased the efficiency of the photocatalytic reaction. When the RhB concentration was high, the efficiency of the photocatalysts was reduced due to insufficient photon energy reaching the active sites. Additionally, intermediate compounds could form during the photodegradation reaction and active radicals could be absorbed instead of interacting with the dye molecules [32]. Figure 5e demonstrates the influence of RhB concentration on the degradation process, indicating that the degradation efficiency remained satisfactory when a concentration of 40 ppm was employed, reaching up to 90.5%.

2.5.6. Comparison of RhB Degradation Methods in the Literature

There has been a recent surge in research efforts aimed at efficiently removing RhB from water through photodegradation. Several Ag_3PO_4-based composite photocatalysts, including Ag_3PO_4@GO, Ag_3PO_4/WO$_3$, Ag_3PO_4/Ag, Ag_3PO_4/ZnO, Ag_3PO_4/N-TiO$_2$, Ag_3PO_4/BiVO$_4$, AgBr/Ag_3PO_4, Ag_2MoO_4/Ag_3PO_4, $NiSe_2$/CdS, $NiSe_2$/BiVO$_4$, etc. [33–46], have been developed and used for RhB degradation under visible light photocatalysis. However, these composites exhibit lower photocatalytic efficiency than our synthesized $NiSe_2$/Ag_3PO_4 photocatalyst, which demonstrated the highest catalytic activity for RhB degradation. Our studies showed that using 30 mg of the $NiSe_2$/Ag_3PO_4 photocatalyst for just 20 min produced a degradation efficiency of 99.5%. The rate constant is important as it provides insights into the reaction mechanism and efficiency of a catalyst. In this study, a rate constant of 0.2275 min^{-1} was observed in the most efficient degradation of a 10 ppm RhB solution, as shown in Table 1.

Table 1. A comparison of the various catalysts for RhB photodegradation reported in the literature.

Catalyst	Catalyst Amount (mg)	Dye Amount (ppm)	Degradation Time (min)	Degradation Efficiency (%)	Rate Constant (min^{-1})	Reference
Ag_3PO_4@GO	50	6	60	99	-	[32]
Ag_3PO_4/WO$_3$	40	5	30	97	-	[33]
Ag_3PO_4/Ag	100	10	90	98	-	[34]
Ag_3PO_4/ZnO	20	10	30	93	0.0895	[35]
Ag_3PO_4/CdSe	25	10	60	99	-	[36]
Ag_3PO_4/N-TiO$_2$	20	10	120	99	0.0194	[37]
Ag_3PO_4/BiVO$_4$	100	10	30	92	0.088	[38]
Ag_2MoO_4/Ag_3PO_4	50	10	12	97	0.3591	[39]
AgBr/Ag_3PO_4	100	10	7	99	-	[40]
$Bi_4Ti_3O_4$/Ag_3PO_4	20	5	30	99	0.1789	[41]
g-C_3N_4/Ag_3PO_4	100	10	10	96	-	[42]
Ag_3PO_4/CdWO$_4$	100	10	5	99	0.71	[43]
CNT/Ag_3PO_4	75	10	12	92.4	0.207	[44]
$NiSe_2$/CdS	50	10	360	85	0.01	[45]
$NiSe_2$/BiVO$_4$	50	10	360	99	0.0149	[46]
$NiSe_2$/Ag_3PO_4	25 25	10 40	20 20	99.9 90.5	0.2275	This Work

2.6. Bisphenol A Optimization Studies

To determine the effectiveness of the newly synthesized photocatalysts for the degradation of BPA, several factors were analyzed and evaluated. These factors included the selection of the catalysts, pH level, the amount of catalyst used, the duration of the process, and the BPA concentration.

2.6.1. Photocatalyst Selection for BPA Degradation

To assess the efficiency of the recently developed catalysts for BPA degradation using the photocatalytic approach, 30 mL of a 5 ppm bisphenol A solution was mixed with 20 mg of each photocatalyst and the photocatalytic activity of the samples was monitored using UV-visible spectrophotometry after exposure for 40 min at 25 °C with continuous magnetic stirring. To choose the optimal catalyst, their efficacy in dye degradation was considered as the determining factor. A decrease in the unique peak of BPA was observed over time, and

it was found that the 20% $NiSe_2/Ag_3PO_4$ composite was an effective photocatalyst for BPA degradation, as shown in Figure 6a.
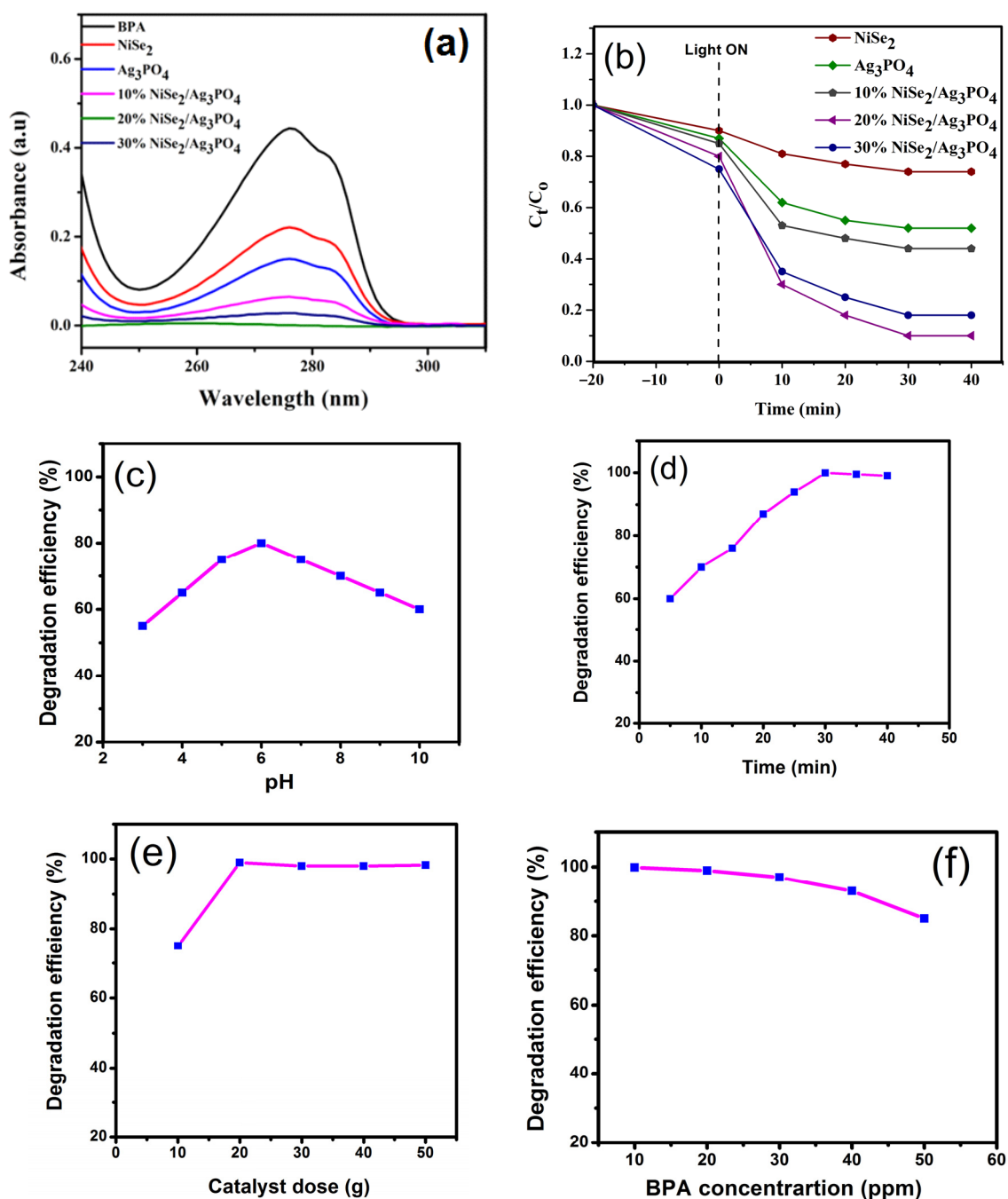

Figure 6. The optimization studies of BPA degradation: (**a**) the UV-Vis spectra for catalyst selection (conditions: catalyst dose = 20 mg; RhB = 5 ppm; time = 40 min); (**b**) the degradation efficiency of various photocatalysts as a function of irradiation time (the other conditions were the same as in (**a**)); (**c**) pH; (**d**) reaction time; (**e**) catalyst dose; (**f**) BPA concentration.

2.6.2. pH Optimization for the Degradation of Bisphenol A

To achieve the maximum degradation efficiency of bisphenol A, a catalyst dosage of 20 mg was used in a 10 ppm BPA solution and the pH was adjusted from 2 to 12 at 25 °C. The concentrations of hydrogen and hydroxide ions present in aqueous environments can affect the surface charges of semiconductor oxides, thereby influencing the potential for

adsorption on surface sites and the reactivity of photocatalysts. Figure 6c demonstrates the significant improvement in degradation efficiency as the pH increased from 2 to 6. However, the efficiency remained constant from pH 6 to 8, then it increased again until it reached a maximum from pH 9 to 12, after which it decreased. In acidic media, the photocatalytic activity of bisphenol A reduced for two main reasons. Firstly, bisphenol A can become protonated in acidic conditions, which negatively affects its ability to accept electron-hole pairs. Secondly, the surface charge of photocatalysts can be altered by acidic pH, resulting in the repulsion of positively charged bisphenol A molecules from the photocatalyst surface, which reduces the amount of bisphenol A available for photocatalytic reaction [47]. BPA has a pKa value that falls within the range of 9.6–10.2, and it was observed that a bisphenolate anion was produced due to BPA ionization at a pH of approximately 9–10 [48]. The zero-point charge of Ag_3PO_4 particles was found to be around 5.4, indicating that the surface charges of Ag_3PO_4 particles were negatively charged in alkaline environments. Under basic pH conditions, there was the possibility of electrostatic repulsion taking place between negatively charged surfaces and anions, leading to a reduction in the frequency of adsorption. As a result, the reactivity of BPA photodegradation on the surface of Ag_3PO_4 particles decreased. Therefore, the removal of BPA was more efficient at neutral pH values compared to acidic or alkaline pH values.

2.6.3. Reaction Time Optimization for the Degradation of Bisphenol A

A series of experiments were conducted to investigate the effect of reaction time on the catalytic activity of the 20 mg catalyst in a 10 ppm BPA solution at pH 6 and 25 °C. The experiments were carried out over different time intervals, ranging from 0 to 40 min. It was observed that BPA removal efficiency increased with the increase in irradiation time, as shown in Figure 6d. The suppression of effective electron-hole recombination could have been the reason for the better catalytic efficiency observed after longer periods of time. Increased exposure to light also enhanced the rate of electron transport. BPA was found to be completely degraded within 30 min; thus, this duration was chosen for bisphenol A degradation.

2.6.4. Catalyst Dose Optimization for the Degradation of Bisphenol A

An experiment was conducted to explore the effect of photocatalyst dosage on BPA degradation under the previously established optimal conditions. The catalyst dosage was changed from 10 mg g to 50 mg. The findings revealed that a greater amount of catalyst increased both the rate of photodegradation and adsorption capacity [49]. Increasing the quantity of photocatalyst resulted in a larger illuminated surface area, as well as a greater number of active sites that were available for the adsorption and degradation of dye molecules. This, in turn, could increase the rate of photodegradation, as demonstrated in Figure 6e. However, there was a slight decrease in efficiency as the catalyst dose increased, possibly due to excessive particles obstructing incident visible light from reaching the catalyst surface.

2.6.5. BPA Concentration Optimization for the Degradation of Bisphenol A

Another study investigated the effect of different concentrations of BPA (ranging from 10 ppm to 50 ppm) on the photodegradation efficiency of the photocatalysts. According to the findings, the highest level of degradation efficiency was attained when the BPA concentration was 10 ppm, while the efficiency decreased with increasing concentrations of BPA. As shown in Figure 6f, the photodegradation process slowed down as the concentration of the dye increased. This could be attributed to the shorter distance that light had to travel to reach the photocatalysts due to the higher concentration of dye, leading to the decrease in the rate of degradation [49]. Increasing the dye concentration augmented its adsorption on the photocatalyst surface, thereby hindering the adsorption of hydroxyl ions and oxygen and, ultimately, inhibiting the photodegradation process.

2.6.6. Comparison of BPA Degradation Methods in the Literature

The literature contains reports of several photocatalysts that have been employed for the photodegradation of bisphenol A. Various Ag_3PO_4-based composites, such as $Ag_3PO_4/LaCoO_3$, Ag_3PO_4/TiO_2, Ag_3PO_4/W, Ag_3PO_4/GO, $CoFe_2O_4/Ag_3PO_4$, etc. [50–56], have been synthesized and employed for the degradation of bisphenol A using visible light photocatalysis. However, our 20% $NiSe_2/Ag_3PO_4$ photocatalyst outperformed these catalysts in terms of the photodegradation of a 20 ppm bisphenol A solution, which took just 30 min using 20 mg of catalyst. The rate constant is important as it provides insights into the reaction mechanism and efficiency of a catalyst. In this study, a rate constant of 0.1266 min^{-1} was achieved with a degradation efficiency of 99.4%, as shown in Table 2.

Table 2. A comparison of the various photocatalysts for BPA photodegradation reported in the literature.

Catalyst	Catalyst Amount (mg)	Dye Amount (ppm)	Degradation Time (min)	Degradation Efficiency (%)	Rate Constant (min^{-1})	Reference
$Ag_3PO_4/LaCoO_3$	25	10	30	81.5	0.08321	[50]
Ag_3PO_4/W	400	20	40	82	0.122	[51]
Ag_3PO_4/TiO_2	50	20	20	95	0.17	[52]
Ag_3PO_4	50	10	10	80.3	-	[53]
Ag_3PO_4/GO	75	10	30	86.4	-	[54]
$CoFe_2O_4/Ag_3PO_4$	25	20	60	91.12	0.03411	[55]
$Bi_2WO_6/BiOI@Ag_3PO_4$	100	20	120	84.8	0.03127	[56]
$NiSe_2/Ag_3PO_4$	20	20	30	99.4	0.1266	This work

2.7. Degradation Kinetics

The degradation kinetics were analyzed to find out the order and rate constant. The Langmuir–Hinshelwood (L-H) model was used for the rate constant determination for the degradation of RhB and BPA [57].

$$-\ln(C_t/C_o) = kt$$

where C_o is the initial pollutant concentration and C_t is the final pollutant concentration after time t. The degradation kinetics of rhodamine B and bisphenol A were determined using the Langmuir–Hinshelwood model, and the pseudo-first-order rate constant "k" was calculated by plotting ln (C_o/C_t) against time (t). The degradation of rhodamine B by the 20% $NiSe_2/Ag_3PO_4$ composite followed pseudo-first-order kinetics with a rate constant of 0.2275 min^{-1}. Similarly, the degradation of bisphenol A by the same catalyst also showed pseudo-first-order kinetics, characterized by a rate constant of 0.1266 min^{-1}, as demonstrated in Figure 7a,b.

2.8. Possible Photodegradation Mechanisms

To investigate the degradation mechanism, we examined the impact of various scavengers on RhB and BPA photodegradation. Figure 8 shows that the use of an electron scavenger ($AgNO_3$) had no significant impact, while the use of a hole scavenger (Na_2SO_3) completely suppressed photocatalytic activity, indicating the essential role of holes in the degradation of RhB and BPA. The addition of ascorbic acid (AA), a superoxide anion scavenger, significantly affected photocatalytic activity, whereas the addition of tert-butanol (TBA), a hydroxyl radical scavenger, had little effect. Hence, the degradation of RhB and BPA was significantly influenced by the presence of superoxide anion radicals, emphasizing their crucial role in the degradation process.
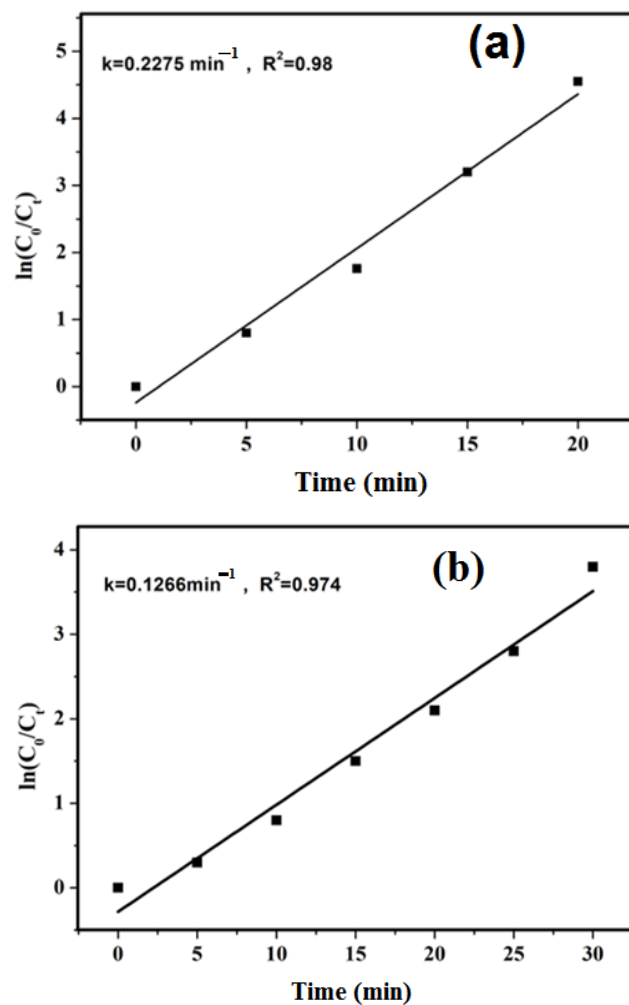
Figure 7. The pseudo-first-order kinetic studies for (**a**) RhB degradation and (**b**) BPA degradation using the 20% $NiSe_2/Ag_3PO_4$ composite.
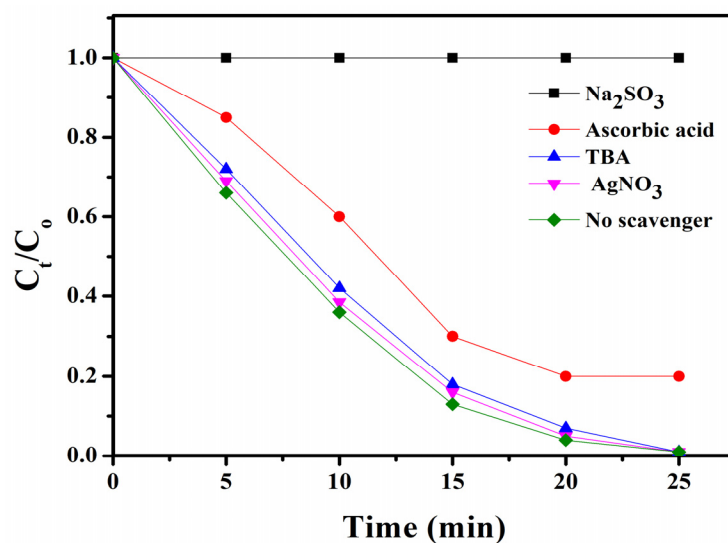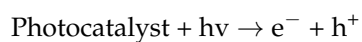

Figure 8. The effect of different scavengers on RhB and BPA degradation.

When light strikes a photocatalyst's surface, electrons and hole pairs are generated as follows [37]:

$$Photocatalyst + h\nu \rightarrow e^- + h^+$$

Ag$_3$PO$_4$ and NiSe$_2$ have different valence band and conduction band potentials. Specifically, the valence band potential of Ag$_3$PO$_4$ is 2.81 eV, whereas that of NiSe$_2$ is 0.75 eV. In contrast, the conduction band potential of Ag$_3$PO$_4$ is -1.21 eV, while that of NiSe$_2$ is 0.45 eV. In NiSe$_2$/Ag$_3$PO$_4$ heterostructures, a Z-scheme is formed, which enables the flow of electrons from the Ag$_3$PO$_4$ conduction band to the NiSe$_2$ valence band. This leads to a system in which the electron-hole recombination from both semiconductors is reduced, allowing them to react with OH$^-$ or O$_2$ to produce reactive species. When these reactive species come into contact with a photocatalyst surface, they interact with adsorbed dyes/pollutants. Oxygen absorbed on a photocatalyst surface can capture electrons produced by irradiation, resulting in the formation of superoxide radicals (as shown in Figure 9) [58].
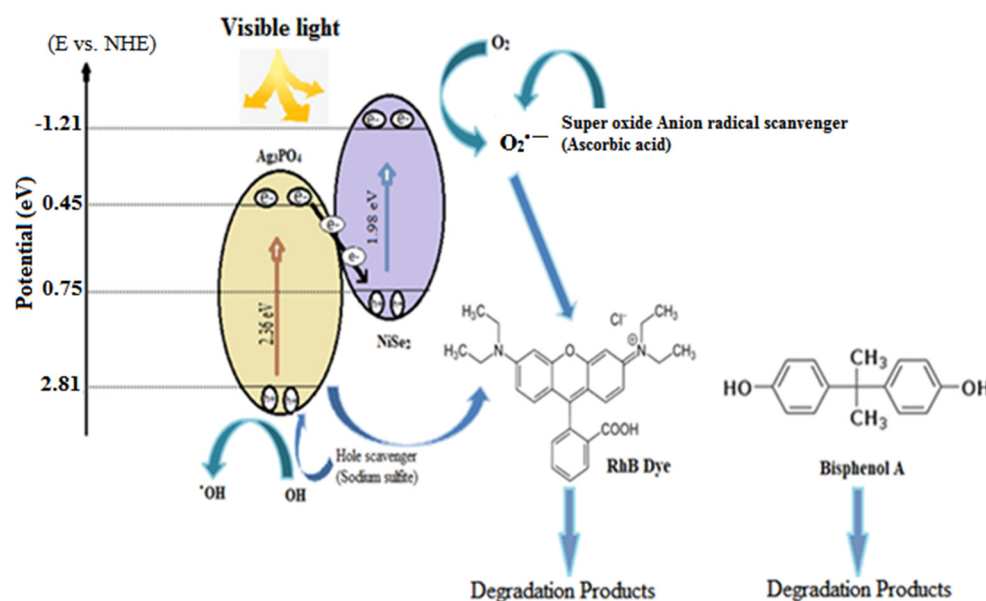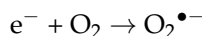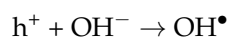
$$e^- + O_2 \rightarrow O_2^{\bullet -}$$

Figure 9. Possible mechanisms for photodegradation.

Hydroxyl radicals can be produced by the absorption of photo-induced holes by surface hydroxyl groups on a photocatalyst's surface [59].

$$h^+ + OH^- \rightarrow OH^{\bullet}$$

The degradation of environmental pollutants is mainly attributed to radicals produced during the photocatalytic process. As mentioned earlier, holes have been found to be crucial for the degradation of BPA and RhB, as evidenced by the scavenger effect [60].

$$\text{Pollutant} + h^+ \rightarrow \text{Degradation products}$$

2.9. Photocatalyst Stability

Stability is a crucial aspect to consider for practical applications of photocatalysts. To evaluate the stability of the pure Ag$_3$PO$_4$ and 20% NiSe$_2$/Ag$_3$PO$_4$ photocatalysts, recycling experiments were performed using RhB dye (10 ppm). As shown in Figure 10, the RhB degradation rate of Ag$_3$PO$_4$ decreased to only 37% after three cycles, indicating a loss in photocatalytic activity. In contrast, the RhB degradation rate of the 20% NiSe$_2$/Ag$_3$PO$_4$ composite was 80% after five cycles, suggesting that the addition of NiSe$_2$ to the composite improved its stability and prevented any significant reductions in photocatalytic activity over multiple cycles.
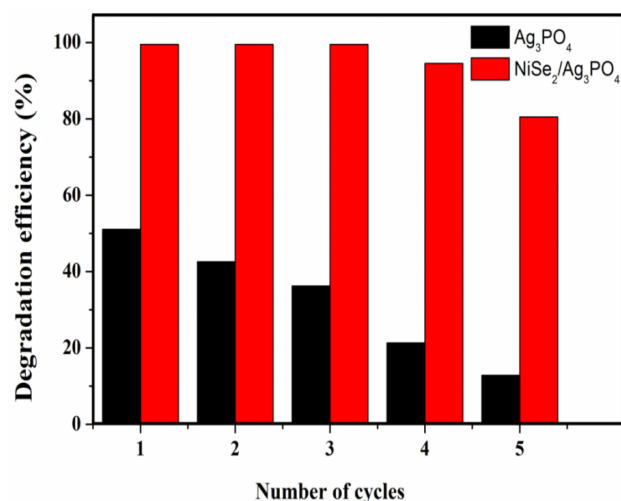
Figure 10. The stability of the photocatalysts under the optimized reaction conditions (light source = 100 watt LED; intensity = 40 k Lux; pressure = 1 atm; temperature = 25 °C; catalyst dose = 30 mg; dye concentration = 10 ppm).

To evaluate the stability of the photocatalysts, the XRD patterns of the 20% $NiSe_2/Ag_3PO_4$ composite were recorded after five reaction cycles. Figure 11 illustrates that the pure Ag_3PO_4 decomposed to form metallic sliver (Ag^*), whereas no signal from metallic Ag was observed in the XRD spectra of the 20% $NiSe_2/Ag_3PO_4$ composite. This indicated that the composite demonstrated higher stability compared to the pure Ag_3PO_4. The absence of metallic silver (Ag^*) signals in the composite suggested that the addition of $NiSe_2$ improved the stability of the Ag_3PO_4, thereby preventing the decomposition and degradation of the photocatalyst during degradation reactions.
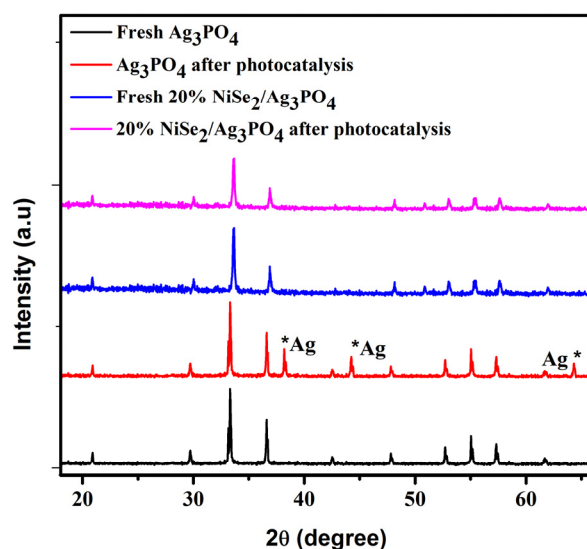

Figure 11. The XRD patterns of fresh and used Ag_3PO_4 and $NiSe_2/Ag_3PO_4$ composite for the degradation of RhB.

3. Experiments

3.1. Materials

The analytical-grade chemicals were provided by Sigma Aldrich, i.e., the sodium borohydride ($NaBH_4$), nickel chloride ($NiCl_2 \cdot 6H_2O$), selenium powder (Se), silver nitrate ($AgNO_3$), disodium hydrogen phosphate (Na_2HPO_4), and ethanol (CH_3CH_2OH). The chemicals provided by Sigma Aldrich were ready for use without requiring any further purification.

3.2. Synthesis of NiSe$_2$

NiSe$_2$ was synthesized using the hydrothermal method. For a typical synthesis, a molar ratio of 1:2 of NiCl$_2$·6H$_2$O to elemental Se was used. First, 0.5 g of Se powder was mixed with 30 mL of distilled water and was sonicated briefly. Next, a reducing agent (0.5 g of sodium borohydride) was added, followed by the addition of the NiCl$_2$·6H$_2$O solution (0.9 g/20 mL) and further sonication. The resulting solution was homogeneous and was transferred to an autoclave. The oven was set to 120 °C and the autoclave was left inside for 12 h. After rinsing the product with distilled water and ethanol, it was dried overnight to obtain nickel selenide powder [15].

The main chemical reaction for the formation of NiSe$_2$ is given below:

$$Ni^{+2} + Se^{-2} \rightarrow NiSe$$

$$NiSe + Se \rightarrow NiSe_2$$
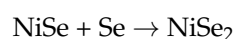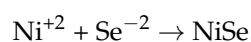
3.3. Synthesis of NiSe$_2$/Ag$_3$PO$_4$ Composites by Hydrothermal Method

A composite of nickel selenide and silver phosphate was synthesized through a hydrothermal process. In a typical process, nickel selenide powder was dispersed in 20 mL of distilled water by sonicating 0.04 g of the material. Then, 1.41 g of disodium hydrogen phosphate and 0.51 g of silver nitrate were added to the mixture, which was subsequently placed in an autoclave with a Teflon lining and heated at 100 °C for 24 h. The final composite was washed three times with water and ethanol. By varying the amount of nickel selenide, three different composite ratios (10%, 20%, and 30% NiSe$_2$/Ag$_3$PO$_4$) were obtained. The same process was used to prepare pure silver phosphate without nickel selenide [36].

3.4. Photocatalytic Performance

The synthesized photocatalysts were used to degrade RhB and BPA under visible light. The light source employed was a 100-watt LED with an output of 40k Lux, as measured by an Extech LT300 light meter. To prevent degradation caused by exposure to light before the start of the experiments or during the preparation of the homogeneous catalyst–dye solutions, the solutions were generally prepared under low light or dark conditions. Furthermore, opaque containers or aluminum foil were used to store the solutions to prevent exposure to light. All experiments were conducted at 25 °C. To perform the experiments, 30 mg of the 20% NiSe$_2$/Ag$_3$PO$_4$ photocatalyst was added to 30 mL of a solution containing RhB (pH 7) and BPA (pH 6). The temperature of the solution was maintained at 25 °C while it was stirred continuously with a magnetic stirrer (Model VELP Scientifica). At predetermined time intervals, 5 mL of the mixture was taken and the photocatalyst was removed via centrifugation. The residual levels of RhB and BPA were assessed by measuring their specific lambda maxima at 554 nm and 275 nm, respectively, using a UV-Vis spectrophotometer (Model UV-1700 SHIMADZU).

$$\text{Degradation Efficiency (\%)} = \frac{(C_o - C_t)}{C_o} \times 100$$

where C_t is the pollutant concentration after irradiation time t and C_o is the initial concentration of the pollutant

4. Conclusions

A highly efficient NiSe$_2$/Ag$_3$PO$_4$ photocatalyst was synthesized using a simple hydrothermal procedure. Both rhodamine B and bisphenol A were rapidly degraded by the synthesized photocatalysts with high efficiency. The degradation rates were nearly 100%, and the 20% NiSe$_2$/Ag$_3$PO$_4$ composite was found to be the most effective at photodegrading rhodamine B and bisphenol A out of the synthesized composite compositions.

The addition of pure nickel selenide into silver phosphate successfully reduced the crystallite size from 86.52 nm to 47.73 nm, leading to the significant enhancement of the photo oxidation stability and capacity of Ag$_3$PO$_4$. Using 20 mg and 30 mg of the

20% NiSe$_2$/Ag$_3$PO$_4$ photocatalyst, rhodamine B and bisphenol A solutions at 10 and 20 ppm were fully photodegraded in just 20 and 30 min, respectively. The pH of the solutions affected the pollutant degradation rate, with bisphenol A being degraded at pH 6 and rhodamine B having the highest photocatalytic degradation rate under neutral pH conditions. Both pollutants followed pseudo-first-order kinetics for photodegradation and hole scavengers could completely stop the degradation process, indicating that holes were the primary cause. The 20% NiSe$_2$/Ag$_3$PO$_4$ composite was the most stable catalyst, exhibited a degradation efficiency of over 80%, and could be used for five cycles.

References

1. Areeb, A.; Yousaf, T.; Murtaza, M.; Zahra, M.; Zafar, M.I.; Waseem, A. Green photocatalyst Cu/NiO doped zirconia for the removal of environmental pollutants. *Mater. Today Commun.* **2021**, *28*, 102678. [CrossRef]
2. Nafees, M.; Waseem, A. Organoclays as Sorbent Material for Phenolic Compounds: A Review. *CLEAN-Soil Air Water* **2014**, *42*, 1500–1508. [CrossRef]
3. Wahab, N.; Saeed, M.; Ibrahim, M.; Munir, A.; Saleem, M.; Zahra, M.; Waseem, A. Synthesis, Characterization, and Applications of Silk/Bentonite Clay Composite for Heavy Metal Removal From Aqueous Solution. *Front. Chem.* **2019**, *7*, 654. [CrossRef] [PubMed]
4. Yousaf, T.; Areeb, A.; Murtaza, M.; Munir, A.; Khan, Y.; Waseem, A. Silane-Grafted MXene (Ti$_3$C$_2$TX) Membranes for Enhanced Water Purification Performance. *ACS Omega* **2022**, *7*, 19502–19512. [CrossRef] [PubMed]
5. Chowdhary, P.; Bharagava, R.N.; Mishra, S.; Khan, N. Role of industries in water scarcity and its adverse effects on environment and human health, Environmental Concerns and Sustainable Development. *Air Water Energy Resour.* **2020**, *1*, 235–256.
6. Ullah, R.; Iftikhar, F.J.; Ajmal, M.; Shah, A.; Akhter, M.S.; Ullah, H.; Waseem, A. Modified Clays as an Efficient Adsorbent for Brilliant Green, Ethyl Violet and Allura Red Dyes: Kinetic and Thermodynamic Studies. *Pol. J. Environ. Stud.* **2020**, *29*, 3831–3839. [CrossRef]
7. Ullah, H.; Nafees, M.; Iqbal, F.; Awan, M.S.; Shah, A.; Waseem, A. Adsorption Kinetics of Malachite Green and Methylene Blue from Aqueous Solutions Using Surfactant-modified Organoclays. *Acta Chim. Slov.* **2017**, *64*, 449–460. [CrossRef]
8. Saeed, M.; Munir, M.; Nafees, M.; Shah, S.S.A.; Ullah, H.; Waseem, A. Synthesis, characterization and applications of silylation based grafted bentonites for the removal of Sudan dyes: Isothermal, kinetic and thermodynamic studies. *Microporous Mesoporous Mater.* **2020**, *291*, 109697. [CrossRef]
9. Kaviyarasu, K.; Kanimozhi, K.; Matinise, N.; Magdalane, C.M.; Mola, G.T.; Kennedy, J.; Maaza, M. Antiproliferative effects on human lung cell lines A549 activity of cadmium selenide nanoparticles extracted from cytotoxic effects: Investigation of bio-electronic application. *Mater. Sci. Eng. C* **2017**, *76*, 1012–1025. [CrossRef] [PubMed]
10. Huang, Y.; Wong, C.; Zheng, J.; Bouwman, H.; Barra, R.; Wahlström, B.; Neretin, L.; Wong, M.H. Bisphenol A (BPA) in China: A review of sources, environmental levels, and potential human health impacts. *Environ. Int.* **2012**, *42*, 91–99. [CrossRef]
11. Rasalingam, S.; Peng, R.; Koodali, R.T. Removal of hazardous pollutants from wastewaters: Applications of TiO$_2$-SiO$_2$ mixed oxide materials. *J. Nanomater.* **2014**, *2014*, 10. [CrossRef]
12. Dou, M.-Y.; Han, S.-R.; Du, X.-X.; Pang, D.-H.; Li, L.-L. Well-defined FeP/CdS heterostructure construction with the assistance of amine for the efficient H2 evolution under visible light irradiation. *Int. J. Hydrog. Energy* **2020**, *45*, 32039–32049. [CrossRef]
13. Yan, Z.; Wang, W.; Du, L.; Zhu, J.; Phillips, D.L.; Xu, J. Interpreting the enhanced photoactivities of 0D/1D heterojunctions of CdS quantum dots/TiO$_2$ nanotube arrays using femtosecond transient absorption spectroscopy. *Appl. Catal. B* **2020**, *275*, 119151. [CrossRef]
14. Cao, Q.; Yu, J.; Cao, Y.; Delaunay, J.-J.; Che, R. Unusual effects of vacuum annealing on large-area Ag$_3$PO$_4$ microcrystalline film photoanode boosting cocatalyst- and scavenger-free water splitting. *J. Mater.* **2021**, *7*, 929–939. [CrossRef]

15. Zhang, X.; Cheng, Z.; Deng, P.; Zhang, L.; Hou, Y. $NiSe_2/Cd0.5Zn0.5S$ as a type-II heterojunction photocatalyst for enhanced photocatalytic hydrogen evolution. *Int. J. Hydrog. Energy* **2021**, *46*, 15389–15397. [CrossRef]

16. Li, L.; Xu, J.; Li, X.; Liu, Z. Reasonable design of roman cauliflower photocatalyst $Cd_{0.8}Zn_{0.2}S$, high-efficiency visible light induced hydrogen generation. *J. Mater. Sci. Mater. Electron.* **2020**, *31*, 10657–10668. [CrossRef]

17. Zhang, Z.; Yin, Q.; Xu, L.; Zhai, J.; Guo, C.; Niu, Y.; Zhang, L.; Li, M.; Wang, H.; Guan, L. Potassium-doped-$C_3N_4/Cd_{0.5}Zn_{0.5}S$ photocatalysts toward the enhancement of photocatalytic activity under visible-light. *J. Alloys Compd.* **2020**, *816*, 152654. [CrossRef]

18. Dashairya, L.; Sharma, M.; Basu, S.; Saha, P. Enhanced dye degradation using hydrothermally synthesized nanostructured Sb_2S_3/rGO under visible light irradiation. *J. Alloys Compd.* **2018**, *735*, 234–245. [CrossRef]

19. Song, Y.-T.; Lin, L.-Y.; Chen, Y.-S.; Chen, H.-Q.; Ni, Z.-D.; Tu, C.-C.; Yang, S.-S. Novel TiO_2/Sb_2S_3 heterojunction with whole visible-light response for photoelectrochemical water splitting reactions. *RSC Adv.* **2016**, *6*, 49130–49137. [CrossRef]

20. Lu, Q.; Yu, Y.; Ma, Q.; Chen, B.; Zhang, H. 2D transition-metal-dichalcogenide-nanosheet-based composites for photocatalytic and electrocatalytic hydrogen evolution reactions. *Adv. Mater.* **2016**, *28*, 1917–1933. [CrossRef] [PubMed]

21. Zhang, J.; Xing, C.; Shi, F. MoS_2/Ti_3C_2 heterostructure for efficient visible-light photocatalytic hydrogen generation. *Int. J. Hydrog. Energy* **2020**, *45*, 6291–6301. [CrossRef]

22. Zhou, Y.; Ye, X.; Lin, D. One-pot synthesis of non-noble metal $WS_2/g-C_3N_4$ photocatalysts with enhanced photocatalytic hydrogen production. *Int. J. Hydrog. Energy* **2019**, *44*, 14927–14937. [CrossRef]

23. McCarthy, C.L.; Downes, C.A.; Brutchey, R.L. Room temperature dissolution of bulk elemental Ni and Se for solution deposition of a $NiSe_2$ HER electrocatalyst. *Inorg. Chem.* **2017**, *56*, 10143–10146. [CrossRef] [PubMed]

24. Shen, Y.; Ren, X.; Qi, X.; Zhou, J.; Xu, G.; Huang, Z.; Zhong, J. Hydrothermal synthesis of $NiSe_2$ nanosheets on carbon cloths for photoelectrochemical hydrogen generation. *J. Mater. Sci. Mater. Electron.* **2017**, *28*, 768–772. [CrossRef]

25. Lv, T.; Wu, M.; Guo, M.; Liu, Q.; Jia, L. Self-assembly photocatalytic reduction synthesis of graphene-encapusulated $LaNiO_3$ nanoreactor with high efficiency and stability for photocatalytic water splitting to hydrogen. *Chem. Eng. J.* **2019**, *356*, 580–591. [CrossRef]

26. Cao, Q.; Li, Q.; Pi, Z.; Zhang, J.; Sun, L.-W.; Xu, J.; Cao, Y.; Cheng, J.; Bian, Y. Metal–Organic-Framework-Derived Ball-Flower-like Porous Co_3O_4/Fe_2O_3 Heterostructure with Enhanced Visible-Light-Driven Photocatalytic Activity. *Nanomaterials* **2022**, *12*, 904.

27. Cao, Q.; Hao, S.; Wu, Y.; Pei, K.; You, W.; Che, R. Interfacial charge redistribution in interconnected network of $Ni_2P–Co_2P$ boosting electrocatalytic hydrogen evolution in both acidic and alkaline conditions. *Chem. Eng. J.* **2021**, *424*, 130444. [CrossRef]

28. Shafi, P.M.; Bose, A.C. Impact of crystalline defects and size on X-ray line broadening: A phenomenological approach for tetragonal SnO_2 nanocrystals. *AIP Adv.* **2015**, *5*, 057137. [CrossRef]

29. Masnadi-Shirazi, M.; Lewis, R.; Bahrami-Yekta, V.; Tiedje, T.; Chicoine, M.; Servati, P. Bandgap and optical absorption edge of $GaAs_{1-x}Bi_x$ alloys with $0 < x < 17.8\%$. *J. Appl. Phys.* **2014**, *116*, 223506.

30. Hameeda, B.; Mushtaq, A.; Saeed, M.; Munir, A.; Jabeen, U.; Waseem, A. Development of Cu-doped NiO nanoscale material as efficient photocatalyst for visible light dye degradation. *Toxin Rev.* **2021**, *40*, 1396–1406. [CrossRef]

31. Li, T.; Zhao, L.; He, Y.; Cai, J.; Luo, M.; Lin, J. Synthesis of $g-C_3N_4/SmVO_4$ composite photocatalyst with improved visible light photocatalytic activities in RhB degradation. *Appl. Catal. B* **2013**, *129*, 255–263. [CrossRef]

32. Liu, R.; Li, H.; Duan, L.; Shen, H.; Zhang, Q.; Zhao, X. The synergistic effect of graphene oxide and silver vacancy in Ag_3PO_4-based photocatalysts for rhodamine B degradation under visible light. *Appl. Surf. Sci.* **2018**, *462*, 263–269. [CrossRef]

33. Zhang, J.; Yu, K.; Yu, Y.; Lou, L.-L.; Yang, Z.; Yang, J.; Liu, S. Highly effective and stable Ag_3PO_4/WO_3 photocatalysts for visible light degradation of organic dyes. *J. Mol. Catal. A Chem.* **2014**, *391*, 12–18. [CrossRef]

34. Huang, K.; Lv, Y.; Zhang, W.; Sun, S.; Yang, B.; Chi, F.; Ran, S.; Liu, X. One-step synthesis of Ag_3PO_4/Ag photocatalyst with visible-light photocatalytic activity. *Mater. Res.* **2015**, *18*, 939–945. [CrossRef]

35. Dong, C.; Wu, K.-L.; Li, M.-R.; Liu, L.; Wei, X.-W. Synthesis of $Ag_3PO_4–ZnO$ nanorod composites with high visible-light photocatalytic activity. *Catal. Commun.* **2014**, *46*, 32–35. [CrossRef]

36. Kim, Y.G.; Jo, W.-K. Efficient decontamination of textile industry wastewater using a photochemically stable n–n type $CdSe/Ag_3PO_4$ heterostructured nanohybrid containing metallic Ag as a mediator. *J. Hazard. Mater.* **2019**, *361*, 64–72. [CrossRef]

37. Khalid, N.; Mazia, U.; Tahir, M.; Niaz, N.; Javid, M.A. Photocatalytic degradation of RhB from an aqueous solution using $Ag_3PO_4/N-TiO_2$ heterostructure. *J. Mol. Liq.* **2020**, *313*, 113522. [CrossRef]

38. Qi, X.; Gu, M.; Zhu, X.; Wu, J.; Wu, Q.; Long, H.; He, K. Controlled synthesis of $Ag_3PO_4/BiVO_4$ composites with enhanced visible-light photocatalytic performance for the degradation of RhB and 2, 4-DCP. *Mater. Res. Bull.* **2016**, *80*, 215–222. [CrossRef]

39. Cao, W.; An, Y.; Chen, L.; Qi, Z. Visible-light-driven Ag_2MoO_4/Ag_3PO_4 composites with enhanced photocatalytic activity. *J. Alloys Compd.* **2017**, *701*, 350–357. [CrossRef]

40. Wang, B.; Gu, X.; Zhao, Y.; Qiang, Y. A comparable study on the photocatalytic activities of Ag_3PO_4, AgBr and $AgBr/Ag_3PO_4$ hybrid microstructures. *Appl. Surf. Sci.* **2013**, *283*, 396–401. [CrossRef]

41. Zheng, C.; Yang, H.; Cui, Z.; Zhang, H.; Wang, X. A novel $Bi_4Ti_3O_{12}/Ag_3PO_4$ heterojunction photocatalyst with enhanced photocatalytic performance. *Nanoscale Res. Lett.* **2017**, *12*, 1–12. [CrossRef] [PubMed]

42. He, P.; Song, L.; Zhang, S.; Wu, X.; Wei, Q. Synthesis of $g-C_3N_4/Ag_3PO_4$ heterojunction with enhanced photocatalytic performance. *Mater. Res. Bull.* **2014**, *51*, 432–437. [CrossRef]

43. Zhang, C.; Wang, L.; Yuan, F.; Meng, R.; Chen, J.; Hou, W.; Zhu, H. Construction of pn type $Ag_3PO_4/CdWO_4$ heterojunction photocatalyst for visible-light-induced dye degradation. *Appl. Surf. Sci.* **2020**, *534*, 147544. [CrossRef]

44. Xu, H.; Wang, C.; Song, Y.; Zhu, J.; Xu, Y.; Yan, J.; Song, Y.; Li, H. CNT/Ag_3PO_4 composites with highly enhanced visible light photocatalytic activity and stability. *Chem. Eng. J.* **2014**, *241*, 35–42. [CrossRef]

45. Shen, S.; Yan, L.; Song, K.; Lin, Z.; Wang, Z.; Du, D.; Zhang, H. $NiSe_2/CdS$ composite nanoflakes photocatalyst with enhanced activity under visible light. *RSC Adv.* **2020**, *10*, 42008–42013. [CrossRef]

46. Shen, S.; Zhang, H.; Xu, A.; Zhao, Y.; Lin, Z.; Wang, Z.; Zhong, W.; Feng, S. Construction of $NiSe_2/BiVO_4$ Schottky junction derived from work function discrepancy for boosting photocatalytic activity. *J. Alloys Compd.* **2021**, *875*, 160071. [CrossRef]

47. Kaneco, S.; Rahman, M.A.; Suzuki, T.; Katsumata, H.; Ohta, K. Optimization of solar photocatalytic degradation conditions of bisphenol A in water using titanium dioxide. *J. Photochem. Photobiol. A Chem.* **2004**, *163*, 419–424. [CrossRef]

48. Kosky, P.G.; Silva, J.M.; Guggenheim, E.A. The aqueous phase in the interfacial synthesis of polycarbonates. Part 1. Ionic equilibria and experimental solubilities in the BPA-sodium hydroxide-water system. *Ind. Eng. Chem. Res.* **1991**, *30*, 462–467. [CrossRef]

49. Koohestani, H.; Sadrnezhaad, S.K. Photocatalytic degradation of methyl orange and cyanide by using TiO_2/CuO composite. *Desalination Water Treat.* **2016**, *57*, 22029–22038. [CrossRef]

50. Guo, J.; Dai, Y.-Z.; Chen, X.-J.; Zhou, L.-L.; Liu, T.-H. Synthesis and characterization of $Ag_3PO_4/LaCoO_3$ nanocomposite with superior mineralization potential for bisphenol A degradation under visible light. *J. Alloys Compd.* **2017**, *696*, 226–233. [CrossRef]

51. Ma, Y.; Li, J.; Jin, Y.; Gao, K.; Cai, H.; Ou, G. The enhancement mechanism of ultra-active Ag_3PO_4 modified by tungsten and the effective degradation towards phenolic pollutants. *Chemosphere* **2021**, *285*, 131440. [CrossRef]

52. Taheri, M.E.; Petala, A.; Frontistis, Z.; Mantzavinos, D.; Kondarides, D.I. Fast photocatalytic degradation of bisphenol A by Ag_3PO_4/TiO_2 composites under solar radiation. *Catal. Today* **2017**, *280*, 99–107. [CrossRef]

53. Katsumata, H.; Taniguchi, M.; Kaneco, S.; Suzuki, T. Photocatalytic degradation of bisphenol A by Ag_3PO_4 under visible light. *Catal. Commun.* **2013**, *34*, 30–34. [CrossRef]

54. Wang, C.; Zhu, J.; Wu, X.; Xu, H.; Song, Y.; Yan, J.; Song, Y.; Ji, H.; Wang, K.; Li, H. Photocatalytic degradation of bisphenol A and dye by graphene-oxide/Ag_3PO_4 composite under visible light irradiation. *Ceram. Int.* **2014**, *40*, 8061–8070. [CrossRef]

55. Zhai, Y.; Dai, Y.; Guo, J.; Zhou, L.; Chen, M.; Yang, H.; Peng, L. Novel biochar@ $CoFe_2O_4/Ag_3PO_4$ photocatalysts for highly efficient degradation of bisphenol a under visible-light irradiation. *J. Colloid Interface Sci.* **2020**, *560*, 111–121. [CrossRef] [PubMed]

56. Chu, Y.; Miao, B.; Zheng, X.; Su, H. Fabrication of flower-globular $Bi_2WO_6/BiOI@Ag_3PO_4$ photocatalyst for the degradation of bisphenol A and cefepime under sunlight: Photoelectric properties, degradation performance, mechanism and biodegradability enhancement. *Sep. Purif. Technol.* **2021**, *272*, 118866. [CrossRef]

57. Kumar, K.V.; Porkodi, K.; Rocha, F. Langmuir–Hinshelwood kinetics—A theoretical study. *Catal. Commun.* **2008**, *9*, 82–84. [CrossRef]

58. Colmenares, J.C.; Luque, R. Heterogeneous photocatalytic nanomaterials: Prospects and challenges in selective transformations of biomass-derived compounds. *Chem. Soc. Rev.* **2014**, *43*, 765–778. [CrossRef]

59. Ahmed, S.; Rasul, M.; Brown, R.; Hashib, M. Influence of parameters on the heterogeneous photocatalytic degradation of pesticides and phenolic contaminants in wastewater: A short review. *J. Environ. Manag.* **2011**, *92*, 311–330. [CrossRef] [PubMed]

60. Ge, M.; Zhu, N.; Zhao, Y.; Li, J.; Liu, L. Sunlight-Assisted Degradation of Dye Pollutants in Ag_3PO_4 Suspension. *Ind. Eng. Chem. Res.* **2012**, *51*, 5167–5173. [CrossRef]